SCIENCE CHINA
Physics, Mechanics & Astronomy

• Article •

July 2025 Vol. 68 No. 7: 274711
https://doi.org/10.1007/s11433-025-2653-2

Scaling law of ultrasonic-induced bubbling toward solid-free air purification

Xiuxing Tang[1,2], Hongyue Chen[1,2], Xiaoliang Ji[1,2], Liang Zhang[1,2], Marco A. B. Andrade[3], Muyang Zhang[1], Jieming Zhang[1], Minghao Zhou[1], Yichen Jiang[4], and Duyang Zang[1,2*]

[1] *School of Physical Science and Technology, Northwestern Polytechnical University, Xi'an 710129, China*
[2] *Shaanxi Liquid Physics Research Center, Northwestern Polytechnical University, Xi'an 710129, China*
[3] *Institute of Physics, University of São Paulo, São Paulo 03001-000, Brazil*
[4] *School of Marine Science and Technology, Northwestern Polytechnical University, Xi'an 710129, China*

Received January 29, 2025; accepted March 27, 2025; published online May 27, 2025

The interaction between ultrasound and the air-liquid interface is widely involved in sonar communication, medical imaging, acoustic detection, etc. In this work, we report an intriguing bubbling phenomenon occurring at the liquid surface exposed to acoustic radiation. The phenomenon can be robustly triggered once the distance between the liquid surface and the acoustic probe is adjusted to multiples of half sound wavelength. It is clarified that the bubbling is attributed to the Helmholtz resonance of the liquid concavity caused by the acoustic radiation force. The sizes of the final obtained bubbles show a universal scaling law with acoustic Bond number and acoustic Reynolds number: $R \approx \lambda \cdot Bo_a \cdot \sqrt{Re_a}$, which is independent of the types of liquids. Moreover, it was found that the bubbling phenomenon showed a significantly enhanced particle absorption ability, thus shedding light on the development of solid filter-free air purification techniques.

ultrasound, air-liquid interface, Helmholtz resonance, air purification

PACS number(s): 43.25.+y, 68.35.Ja, 47.35.Rs

Citation: X. Tang, H. Chen, X. Ji, L. Zhang, M. A. B. Andrade, M. Zhang, J. Zhang, M. Zhou, Y. Jiang, and D. Zang, Scaling law of ultrasonic-induced bubbling toward solid-free air purification, Sci. China-Phys. Mech. Astron. **68**, 274711 (2025), https://doi.org/10.1007/s11433-025-2653-2

1 Introduction

The interaction between ultrasound and the air-liquid interface has broad applications in sonar communication [1], medical imaging [2], and acoustic detection [3]. Many efforts were made to study the ultrasonic reflection and transmission at the air-liquid interface. For instance, evanescent waves [4], membrane-type metasurface [5], and resonant bubbles [6] were used to enhance the acoustic transmission. The metamaterial fence [7], zero-mass metamaterial [8], and lotus metasurface [9,10] were also proposed for the effective acoustic transmission. Microbubbles are introduced to human tissues as contrast agents to increase ultrasonic reflection and improve the quality of ultrasonic imaging [11-13]. Although transmission and reflection have been extensively studied, the mechanical effects of ultrasound on the gas-liquid interface have rarely been reported. Momentum exchange occurs when ultrasound encounters with the air-liquid interface, which results in acoustic radiation force to the interfaces [14]. Driven by the acoustic radiation force, a

*Corresponding author (email: dyzang@nwpu.edu.cn)

water pool surface can be depressed, thus leading to an intriguing bubbling phenomenon [15,16]. However, the underlying mechanism for the unique surface bubbling is far from being understood, for instance, why closure of the liquid surface is triggered by the acoustic radiation force has not been clarified yet.

Besides the interface dynamics, the action of ultrasound may also influence the physical/chemical processes involved with liquid interfaces, for instance, ultrasonic emulsification [17] and cleaning [18]. It has been reported that the air-liquid interface has the ability to capture solid particles [19], which plays an essential role in multiphase reactions and flotation processes [20,21]. However, it remains to elucidate whether and how the particle captured by the air-liquid interface is influenced by the applied sound field.

In this work, the ultrasound was exerted to the air-liquid interface at varied distances. We focused on how the surface bubbling was triggered by the ultrasound field. It was found that the bubbling phenomenon occurred only when the ultrasound was applied at distances of multiples of half sound wavelength to the liquid surface. We have proposed a scaling law to describe the relation between bubble size, liquid properties, and working parameters. Moreover, the acoustic bubbling phenomenon shows a significant ability to enhance the absorption of particles, which provides a promising air purification method without using any solid filters.

2 Materials and methods

2.1 Materials

Pure water, silicone oil (viscosity μ = 0.1 and 60 Pa s), and SDS (sodium dodecyl sulfate) solution of 0.2, 0.6, and 1.0 CMC (critical micelle concentration) were used as the bath liquid, respectively. The water was purified with an Ultrapure Water System (EPED, China), and all other materials were purchased from Aladdin Industrial Corporation, China. The liquid viscosity was measured with a stress-controlled rheometer (Physica MCR 302; Anton Paar, Germany). The σ was assessed using an Optical Surface Analyzer (LSA100-O2, China).

2.2 Experimental setup and procedure

In the experiments, an ultrasonic probe (diameters Φ, ranging from 6 to 25 mm) was positioned vertically above the surface of a liquid pool (100 mm depth with surface area 200 mm×200 mm) with an adjustable distance H (Figure 1(a)). The working frequencies f of the ultrasonic probe used in the experiments were 20.5, 30.0, and 40.0 kHz, respec-

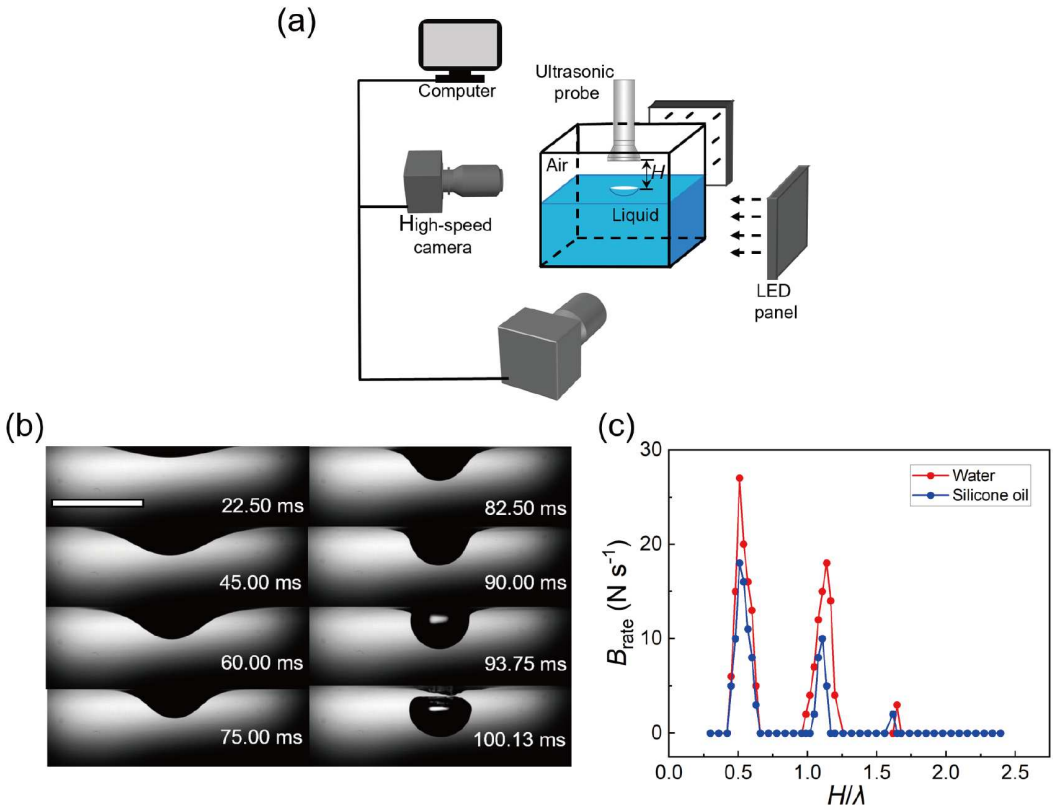

Figure 1 (Color online) Bubbling phenomenon induced by ultrasound. (a) Experimental setup. (b) Bubble formation on the water surface. The scale bar represents 10 mm. (c) Bubble formation rate (B_{rate}) as a function of H scaled by sound wavelength λ.

tively (sound wavelength 16.8, 11.5, 8.6 mm). The vibration velocity amplitudes of the ultrasound of 20.5 kHz (0.41 m/s), 30 kHz (0.29 m/s), 40 kHz (0.2 m/s) were measured with a Doppler laser vibrometer (Vector-High-Speed, Germany), which was used to calculated the RMS acoustic velocity v_{rms}. During the experiments, H was adjusted in the range of $0 < H < 2.5\lambda$ (λ, the wavelength of ultrasound) with precise control. All the experiments were performed at room temperature of ~25°C and a relative humidity of ~40%.

The shape evolution of the liquid surface upon ultrasound was recorded using a high-speed camera (Photron Fastcam Mini UX100, Japan), illuminated by an LED panel. We used a frame rate of 8000 frames per second and an image resolution of 1024 × 762 pixels. The acoustic streaming between the acoustic probe and the air-liquid interface was illuminated by a sheet laser (MGL-N-532A), and the water mist generated by the nebulizer was used as tracer particles.

The obtained images were further processed using Fiji (ImageJ) to obtain the profile and geometry of the liquid surface. To understand the time variation of the volume of the concavity, the recorded images were analyzed using MATLAB 2021b with an in-house compiled code. Based on the determination of concavity boundaries, the volume could be treated as the total volume of cylinders surrounded by each layer of pixels.

2.3 Sound field simulations

The sound field involved in the experiments was simulated by the pressure acoustics module of COMSOL Multiphysics 5.6. For the simulation of sound pressure and acoustic radiation pressure, a two-dimensional axisymmetric model was employed. The boundary of the simulation domain is located between the boundary of the acoustic probe and the liquid surface. The sketch was obtained from the actual size and shape of the experimental conditions. The simulation domain was determined by the geometry of the area between the acoustic probe and liquid pool, where the liquid surface was configured as a continuity boundary and the side wall was set as the radiation boundary condition. The entire simulated domain was meshed by free triangular, and the user's predefined size was set to ultrafine. The residual convergence based on iteration is used for a convergence check. The boundary acoustic pressure was restrained by the Helmholtz equation: $\nabla\cdot\left(-\frac{1}{\rho_0}\nabla p\right)-\frac{p\omega^2}{\rho_0 c_0^2}=0$. The acoustic medium was air (density $\rho_0 = 1.18$ kg/m^3, sound velocity $c_0 = 346.12$ m/s) and water (density $\rho = 998.2$ kg/m^3, sound velocity $c_{\mathrm{water}} = 1495.33$ m/s).

For the simulation of acoustic absorption, the cavity encapsulated by a water shell was placed in a waveguide tube filled with air. The contour line of the sample that was taken from high-speed camera pictures was rotated to create the model of the cavity. The above and below faces of the tube were designated as the "radiation boundary condition", while the side walls were specified as hard boundaries. A planar harmonic wave of 1 Pa was introduced into the simulated domain through the radiation boundary condition in the simulation at the above face of the waveguide, and a zero radiation boundary condition was applied to the below face. The acoustic absorption efficiency was derived by analyzing the transmission and sound field distribution in the tube, and the sound pressure and velocity of the medium particles in the air cavity could be obtained by invoking the simulation results.

2.4 Air purification and MGV analysis

In a closed chamber filled with smoke generated by a smoke generator, an emblem was affixed to the bottom of the chamber, and the adsorption of aerosol particles was monitored using the mean gray value (MGV) of the images. The aerosol gas (the particle size ranges from 0.1 to 1 μm, and the average density of the particles is (1120±40) kg/m^3) was generated by an aerosol generator (LB-3300, LuBo Ltd, Qingdao, China). The aerosol gas was injected into the experimental container (200 mm × 200 mm × 200 mm with a 50 mm depth pure water pool inside) with a computer-controlled peristaltic pump. Before air purification, the same amount of aerosol gas (volume 2 L) was injected into the container. The air purification process was recorded using a single lens reflex (SLR; DS126631; Canon) camera with a macro lens (FF 25 mm F2.8 Ultra Macro 2.5-5.0x, LAOWA). To build the relationship between the obtained images and air purification efficiency, it is necessary to obtain the MGV of the images which was analyzed using MATLAB 2021b with an in-house compiled code. The photos were transferred into a 256 gray-scale image via gray processing, where the gray value is 0 for black pixels and 255 for white pixels. The MGV of the images was obtained from the integration of the corresponding pixels in the contour area. The purification efficiency of the aerosol gas is measured by the transparency of the aerosol gas, which is represented by the MGV of the images.

3 Results and discussion

3.1 Shape evolution of the air-liquid interface under acoustic radiation

The shape evolution dynamics of the liquid surface strongly depended on the ultrasonic probe-liquid surface distance H. It was found that ultrasonic atomization occurred when the ultrasonic probe was positioned too close to the liquid surface, i.e., H ranging from 0 to $1/8\lambda$ (0-2.1 mm). In this range, the liquid surface tended to be attracted to the acoustic probe,

and the liquid atomization was triggered once the liquid surface contacted the probe, where tremendous micron-sized droplets were ejected from the contact position [22] (Movie S1). At larger H, i.e., $1/8\lambda < H \leqslant 2\lambda$ (2.1 mm < $H \leqslant$ 33.6 mm), the acoustic atomization was eliminated and a stable concave profile of the air-liquid interface was evidenced, indicating downward depression effect caused by ultrasound [15]. Moreover, at appropriate H (multiples of half sound wavelength $\lambda/2$, λ, $3\lambda/2$ (8.4, 16.8, 25.2 mm)), the concavity of the liquid surface further evolved into a closed bubble which pinched off downward into the bulk liquid (Figure 1(b), Movie S2). The formed bubbles were finally floated up to the liquid surface, and could be arranged into ordered bubbles with the stabilization of SDS (Movie S3). The bubble formation rate B_{rate}, i.e., the number N of formed bubbles per second, significantly depended on H (Figure 1(c)), where the peak of B_{rate} appeared at multiples of $\lambda/2$ and became smaller at larger distances. This is in line with that the acoustic power density in a Helmholtz horn reaches its peaks at multiples of $\lambda/2$ [23]. If H was larger than 2λ, bubbles could not be formed anymore because with a longer distance, the sound pressure between the probe and the reflection surface considerably decreased due to the enhanced sound wave propagation into the surrounding medium [24].

3.2 Dynamics of bubble formation

Since the acoustic bubbling phenomenon is a subsequent process of liquid surface concavity caused by acoustic radiation, to clarify the bubbling mechanism, the time evolution of the geometry of the concavity, i.e., its width w, depth d, and volume V, was analyzed quantitatively (Figure 2(a)). The acoustic radiation pressure P_{A} exerted on the concavity surface was calculated based on the King's theory which can be applied to any object that scatters sound waves [25], in which $P_{\text{A}} = \frac{1}{\rho_0 c^2}\langle p^2 \rangle - \frac{1}{2}\langle v^2 \rangle$ (where c is the sound speed, p is the sound pressure, and v is the particle velocity of the medium). During the indentation stage, the depth d of the concavity was increased, driven by the acoustic radiation, which was also associated with an increase in width w. This is because at this stage, the downward P_{A} (Figure 2(b)) is

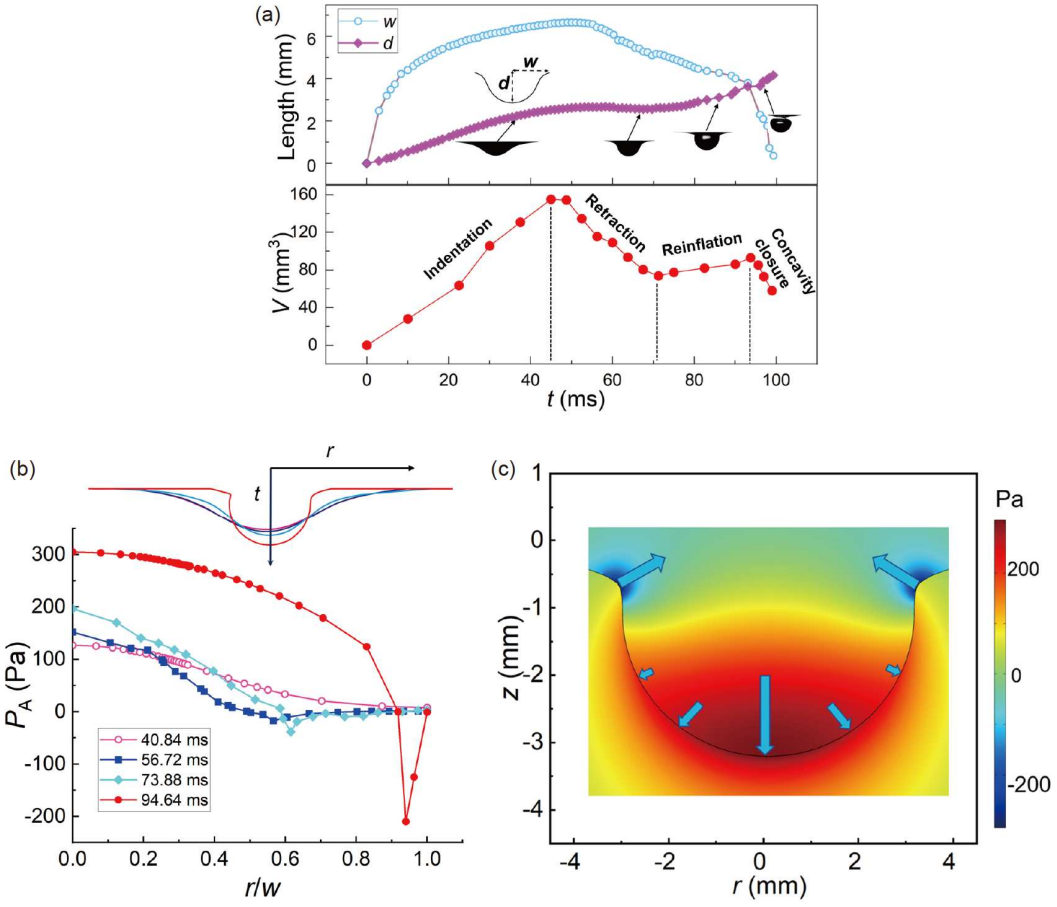

Figure 2 (Color online) Shape evolution acoustic of the concavity on the water surface ($H = \lambda$). (a) Time variation of depth d, width w, and volume V of the concavity. (b) Distribution of acoustic radiation pressure on the water surface at different times (simulation), the horizontal position r is scaled by the width w of the concavity. (c) Distribution of acoustic radiation pressure of the concavity where negative pressure is formed at the concavity neck zone (94.64 ms, simulation), z represents the vertical position measured from the bulk surface.

greater than the sum of hydrostatic pressure ρgd and Laplace pressure P_{L} ($P_L = \frac{2\sigma}{\kappa}$, where σ is the surface tension, κ is the curvature radius at the bottom of the concavity). Once the concavity reached an appropriate shape, negative acoustic radiation appeared at the concavity opening zone (Figure 2(b), square data), resulting in the retraction of the concavity edge. Importantly, rapid closure of the surface concavity occurred at the last stage, just before the bubble formation. This is because the significantly enhanced negative acoustic radiation pressure (suction effect) was exerted at the neck zone (Figure 2(c)), although, why the strong negative pressure appeared at the concavity neck zone remains to be elucidated.

3.3 Acoustic resonance mechanism

To test if the acoustic-induced bubbling is a universal phenomenon, similar experiments were performed with a series of acoustic probes of varied diameters (10/15/25 mm) and for different liquids (water, silicone oil, and SDS solution). It was found that for all these different systems, the bubbling phenomenon occurred in a similar manner, characterized by the formation of a surface concavity and its rapid closure at the last stage. It is worth noticing that in all these experiments, the depth of the concavities d reaches a fixed maximum value ~$\lambda/4$ (Figure 3(a)), which indicates that ultrasound plays an essential role in the maximum depth of the concavity. This observation implies that the bubbling phenomenon may be related to the geometry of the surface concavity, suggesting the occurrence of acoustic resonance at an approximate size and geometry. To verify this hypothesis, the profile of the concavity corresponding to the onset of its closure was extracted, thus, the geometry of the air cavity, which may resonate with the sound field, was obtained. The acoustic absorption spectrum of the air cavity was calculated, where a sharp absorption peak at ~20.7 kHz was evidenced (Figure 3(b)), which is in good agreement with the working frequency of the acoustic probe. In this case, the air cavity showed a significantly enhanced energy density inside (inset

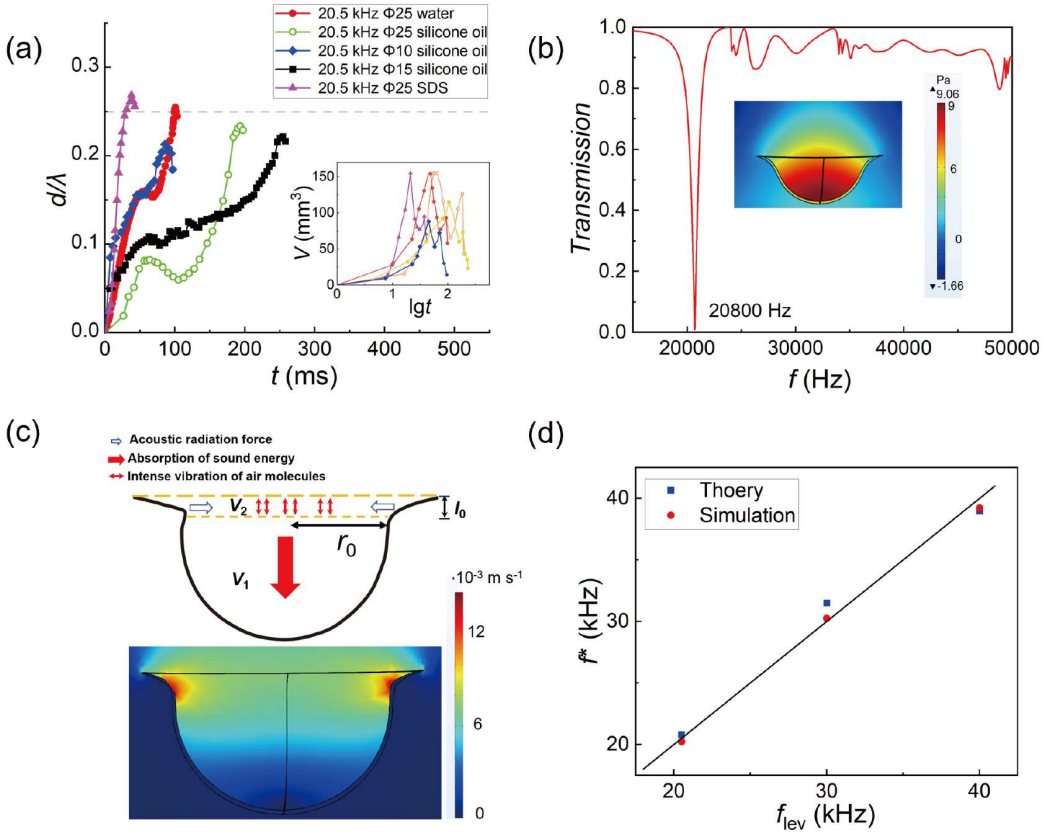

Figure 3 (Color online) Resonance mechanism of the cavity with ultrasound. (a) Time variation of the concavity depth d in different systems, the inset illustration shows that in all these experiments, the volume of concavities seems to experience a similar reinflation stage. The horizontal axis of the inset illustration is calculated by the logarithm base 10. (b) Acoustic absorption simulation of the air cavity. The inset illustration is the distribution of sound pressure. (c) Geometry of the air cavity corresponding to the Helmholtz resonance, which is usually characterized by a deep cavity with volume V_1 and a wide opening with volume V_2, where the radius of the cavity is r_0 and the depth of the opening is l_0. The below illustration shows the vibration velocity distribution of the medium particles during resonance, in which the maximum vibration velocity appeared at the cavity neck zone. (d) Calculation of acoustic resonance frequency, f_{lev} is the acoustic frequency used in the experiments.

of Figure 3(b)), confirming the occurrence of resonance in the air cavity.

It remains to explain the resonance mechanism of the air cavity formed by the concavity of the liquid surface. As shown in the inset graphic of Figure 3(b), the cavity has a low sound pressure at its opening, whereas high pressure inside, analogous to the traditional Helmholtz resonators [26]. Based on the geometry of the air cavity extracted from experimental observation (Figure 3(c)), the Helmholtz resonance of the air cavity can be analogous to an inductor-capacitor circuit resonance. The cavity acts as the capacitor with capacitance $C_0 = \frac{V_1}{\rho_0 c^2}$, and the neck is considered as the inductor with inductance $L_0 = \frac{\rho_0 d_{\text{eff}}}{s_{\text{neck}}}$, where $d_{\text{eff}} = 1.8\sqrt{2r_0} + l_0$ (Figure 3(c)) is the effective depth of the cavity and s_{neck} is the area of the wide opening. In the present work, s_{neck} was calculated by $\frac{V_2}{l_0}$ to represent the effective area of the funnel-shaped opening. Thus, the resonance frequency f_{H} of the concavity, a unique liquid-surrounded Helmholtz resonator, in the present can be obtained based on the inductor-capacitor circuit resonance theory [27], which can be written as:

$$f_{\text{H}} = \frac{1}{2\pi\sqrt{C_0 L_0}} = \frac{c}{2\pi\sqrt{\frac{V_1 l_0\left(l_0+1.8\sqrt{2r_0}\right)}{V_2}}}. \quad (1)$$

The resonant frequencies f_{H} calculated using eq. (1) and that obtained from acoustic simulation both are in good agreement with the working frequency f_{lev} of the levitator (Figure 3(d)), indicating that the air cavity at the liquid surface can be treated as a Helmholtz resonator and the acoustic-induced bubbling indeed took place via a Helmholtz resonance mechanism. Because of the Helmholtz resonance, the medium particles exhibit the highest vibration velocity at the neck zone of the cavity, which in turn results in the strong negative radiation pressure (suction effect) responsible for the rapid concavity closure.

3.4 Scaling law of the bubble size

The final bubble size depends on the sound field and liquid properties, although the physical mechanism for the bubbling process is the same. The acoustic bubbling in the work originates from the Helmholtz resonance of the acoustic-depressed concavity, in which the size of the concavity is overally determined by the probe diameter Φ and working frequency f_{lev}, and in turn for the size of the obtained bubbles (Figure 4(a) and (b)). For the liquid properties, higher μ and σ could lead to smaller bubble size (Figure 4(c) and (d)) due to enhanced sound energy consumption caused by viscous dissipation and bubble surface energy, respectively.

To gain a quantitative description of the bubble size obtained from the acoustic bubbling, we proposed a scaling analysis of the bubble size data. From an energy perspective, the intrinsic physics picture involved in the acoustic bubbling process is that the sound energy was continuously transformed into the surface energy of the bubbles associated with viscous dissipation in both the bulk liquid and the air. Therefore, the competition between acoustic radiation force and surface tension, which can be described by the acoustic Bond number $Bo_a\left(\frac{2v_{\text{rms}}^2\rho_0 r_0}{\sigma}\right)$, plays an essential role in the

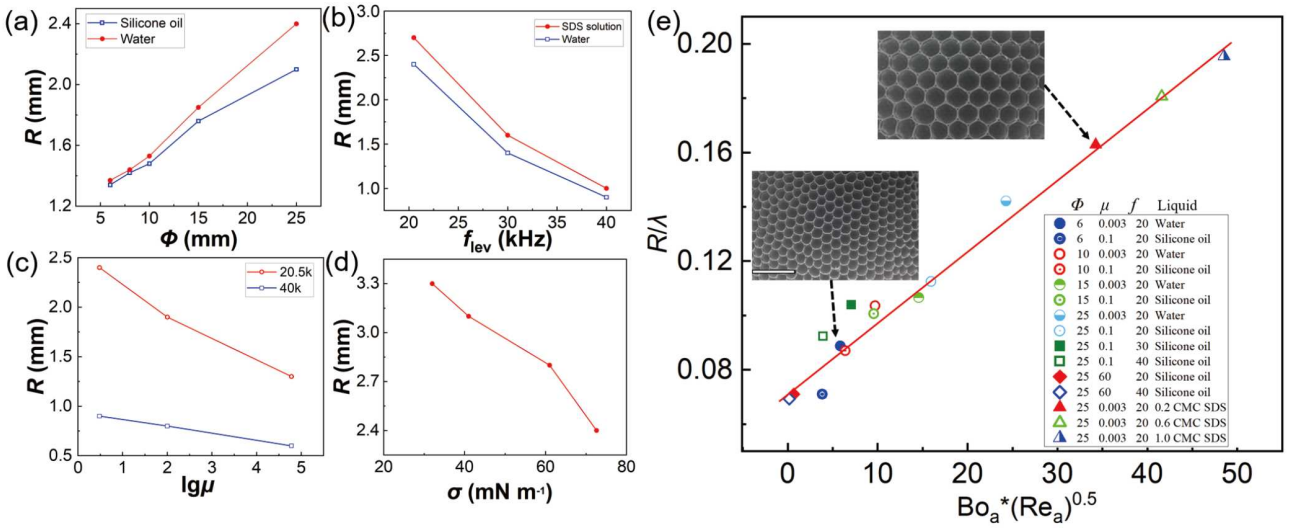

Figure 4 (Color online) Bubble radius affected by experiment parameters. All the experiments were performed when $H = \lambda$. (a)-(d) Variation of the bubble radius with the acoustic probe diameter Φ, liquid viscosity μ (MPa s), acoustic frequency f, and liquid surface tension σ. (e) The dimensionless bubble size rescaled by the acoustic Reynolds number and acoustic Bond number. The red line is the fitted function. Two inset illustrations are typical bubble arrays with controlled size, which is in good agreement with the calculated results using the scaling law.

entire process [28]. Moreover, the viscous dissipation in sound field can be calculated by the acoustic Reynolds number [25] $Re_a = \frac{c^2\rho_0}{\omega\mu\left(\frac{\xi}{\mu}+\frac{4}{3}\right)}$, where $\omega = 2\pi f$ is the angular frequency and ξ is the bulk viscosity (characterizing the relationship between the resistance to an object and the rate of its volume change). By considering both Bo_a and Re_a, and reducing the bubble size by sound wavelength λ, the data in Figure 4(a)-(d) were replotted in Figure 4(e), in which all the data were excellently collapsed into a master curve. Therefore, it is obtained that

$$R \approx \lambda \cdot Bo_a \cdot \sqrt{Re_a}\,. \tag{2}$$

The scaling law of the bubble size in eq. (2) suggests that the bubble size can be predicated accurately and adjusted by the sound field or the liquid properties, thus providing a promising bubbling approach with controlled bubble size.

3.5 Air purification

We further explored the aerosol particle absorption behavior of this unique acoustic bubbling phenomenon (Figure 5(a)), since the air-liquid interface exhibits a strong ability to adsorb macro/nano particles [29,30] and shows promising potential for air purification [31]. Our experimental results demonstrated that the aerosol particles could be effectively adsorbed by the air-liquid interface within 40 s with the presence of surface bubbling (Figure 5(b)-(ii)). By contrast, without the action of sound field, in the same duration, the aerosol particles were almost remained in the air since the transparency of image (Figure 5(b)-(iv)), estimated by the MGV, kept unchanged (Figure 5(c)). It would take nearly 1000 s to achieve a similar particle absorption result as that under acoustic bubbling for 40 s. Moreover, when exposed to ultrasound but without bubbling, i.e., $H \neq \lambda/2$, λ, $3\lambda/2$, the aerosol particles were partly adsorbed by the air-liquid interface within 40 s Figure 5(b)-(iii)). By comparing the results of Figure 5(b)-(i) and Figure 5(b)-(ii), the acoustic-induced surface bubbling significantly enhanced the aerosol particle absorption rate at the air-liquid interface.

It remains to explain why the acoustic bubbling process results in remarkably enhanced particle adsorption ability. Generally, the particle adsorption rate of the liquid surface is

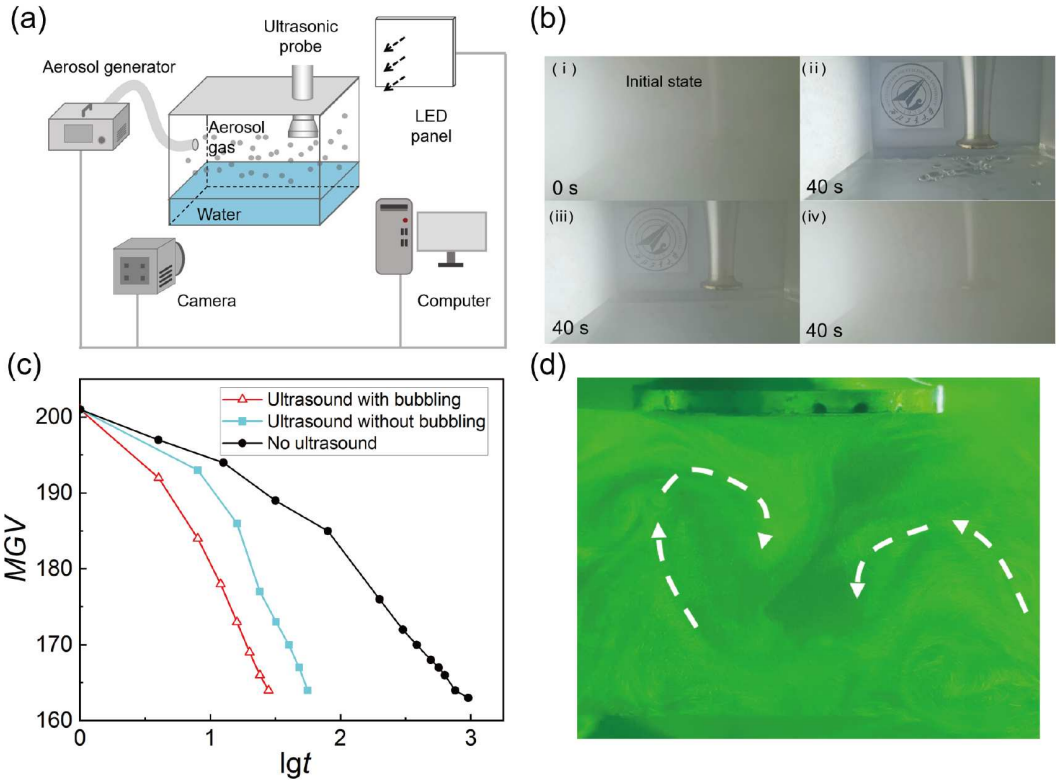

Figure 5 (Color online) Enhanced aerosol particle adsorption via acoustic-surface bubbling. (a) Experimental setup. (b) Air purification via different approaches: (i) the initial state of the working box with the injected aerosol particles suspended in the air, where the transparency is so low that the acoustic probe in the box can hardly be observed; (ii) with acoustic-induced bubbling for 40 s ($d = 3\lambda/2$), where the injected aerosol particles were effectively absorbed thus the acoustic probe could be clearly observed; (iii) exposed to ultrasound but without bubbling for 40 s ($d = 7\lambda/4$), where the injected aerosol particles were partly adsorbed and the transparency of the injected aerosol gas was increased compared with the initial state; (iv) no sound field for 40 s, where the transparency of the injected aerosol gas remained the same of the initial state. (c) MGV analysis of the images under different conditions. (d) The acoustic streaming between the probe and the air-liquid interface.

determined by two stages: (1) how fast the particles reach and contact with the liquid surface (stage I); and (2) how fast the contacted particles are trapped by the air-liquid interface (stage II). As revealed by the previous investigation, the particles trapping process (stage II) is quite fast, in the timescale of ms [31]. This indicates that the limitation for particle adsorption rate would depend on the particle approaching and contacting process (stage I). Without the sound field, the contact between the aerosol particles and the liquid surface is mainly dependent on the thermal diffusion of the particles following the Brownian motion law [32]. However, with the action of sound field, notable acoustic streaming was stimulated between the ultrasonic probe and the liquid surface (Figure 5(d), Movie S4), which drove the particle to impact onto the liquid surface at a speed of ~0.2 m/s. The acoustic streaming is responsible for the enhanced particle absorption rate. Moreover, with the action of bubbling process, the rapidly closure of the liquid surface (concavity edge) and the high v_{rms} at the neck zone of the concavity, lead to a higher particle impact velocity, ~0.5 m/s, which would further accelerate the contact between aerosol particles and the liquid surface and in turn the particle absorption rate.

3.6 Discussion

A similar surface bubbling phenomenon is also frequently observed when the liquid surface is impacted by a droplet or a solid body [24,33]. The impact of a liquid droplet can lead to the formation of a bubble through either a pinch-off mechanism of the downward elongated air cavity or an entrapment mechanism due to the merging of the impact-induced liquid crowns [34,35]. To realize the process, the impact usually needs a sufficiently large Weber number. For the impact of a solid, the appearance of a bubble also needs a threshold velocity, which may depend on the wettability of the impacting body [36,37]. However, in our work, the closure of the liquid surface concavity is driven by the significant negative acoustic radiation pressure exerted at the neck zone owing to the Helmholtz resonance, therefore, not requiring intense impact from other objects.

It should be noted that the surface bubbling is an inevitable result of the liquid surface shape evolution driven by sufficiently strong acoustic radiation. In the process, gravity and surface tension of the liquid tend to impede the indentation of the surface, which enhances the total gravitational potential and surface energy. However, the concave surface exhibits a stronger sound absorption [33], thus leading to an increase in acoustic radiation pressure to promote further indentation. Once the critical shape of the concavity is obtained, the acoustic Helmholtz resonance is triggered inside. In the resonance stage, gravity plays a little role in the scaling law of bubble size since the process is mainly determined by the interplay between ultrasound and the geometry of the concavity.

Although classical Helmholtz theory assumes an ideal geometry of the cavity, its core principle is based on the coupling resonance of the elastic vibration of the air (the volume of the cavity) with the inertial mass (the neck column of air). As long as the structure meets the following two key conditions [38]: (1) effective sealing of the cavity: capable of providing sufficient aeroelastic stiffness which is inversely proportional to the cavity volume; (2) equivalent neck structure: the inertial mass of the air column formed by the narrow passage which is related to neck length and cross-sectional area. In the present work, the medium particles exhibit the highest vibration velocity at the neck zone of the cavity, and the concavity absorbs sound energy, converting it into the surface energy of the bubble. Thus, even if the concavity has an irregular shape, it can be considered a Helmholtz resonator because its acoustic properties are still determined by the above two dominant factors.

The acoustic-induced surface bubbling approach reported in the present work can not only fabricate bubbles or bubble arrays of expected size, but also significantly enhance the mass transfer from air to liquid. This is mainly attributed to the presence of acoustic streaming between the acoustic probe and the liquid surface. Moreover, the Helmholtz resonance itself also enhances the impact velocity between medium particles and the liquid surface, which is favorable for the mass transfer. Based on the significantly enhanced aerosol particle absorption via acoustic-induced surface bubbling, a potential solid filter-free air purification system that solely uses water as filter medium can be built. This solid filter-free air purification system would be environment friendly [31].

Our ultrasonic system provides digitally controlled power output, functioning at approximately 35 W during experiments. After ten minutes of operation, a cleaning efficiency of higher than 95% was achieved. In terms of scalability, our approach facilitates broader application scenarios by allowing the replacement of the liquid pool. For example, hydrogen peroxide or ethanol solutions can be employed for disinfection purposes, whereas sodium hydroxide solutions effectively absorb hydrogen sulfide gas. In high-risk environments such as mining operations and industrial facilities, the liquid filtration medium exhibits superior practicality over solid filter materials due to its ease of replacement. The system ensures continuous operation through infrequent replenishment of liquid consumables and promotes the possibility of permanent application without the need to replace solid filters.

The acoustic probes utilized in the present work are all flat. If curved probes were used instead, the geometric focusing effect would concentrate the sound energy in the focal region, potentially enhancing bubble yield significantly.

Nevertheless, this would not have an impact on the bubble size because bubble formation is determined by Helmholtz resonance.

4 Conclusion

In conclusion, it has been found that an acoustic induced bubbling phenomenon at the air-liquid interface can be triggered when the ultrasound is exerted to interface at distances of multiples of $1/2\lambda$. The bubbling is attributed to the Helmholtz resonance of the acoustic induced liquid surface concavity, which results in a strong negative acoustic radiation force at the neck zone of the concavity, thus leading to its rapid closure and formation of the bubble. The size of the obtained bubble follows a scaling law: $R \approx \lambda \cdot Bo_a \cdot \sqrt{Re_a}$. It has been found that the aerosol particles' adsorption at the air-liquid interface can be significantly enhanced via the acoustic streaming and surface bubbling owing to Helmholtz resonance. Our results give insights into the interaction between ultrasound and air-liquid surface, providing a new method for air purification without using any solid filters.

This work was supported by the National Natural Science Foundation of China (Grant Nos. 12272314, and 11972303).

Conflict of interest The authors declare that they have no conflict of interest.

Supporting Information

The supporting information is available online at http://phys.scichina.com and https://link.springer.com. The supporting materials are published as submitted, without typesetting or editing. The responsibility for scientific accuracy and content remains entirely with the authors.

1 F. Boulogne, F. Restagno, and E. Rio, Phys. Rev. Lett. **129**, 268001 (2022).
2 Z. Jian, M. A. Channa, A. Kherbeche, H. Chizari, S. T. Thoroddsen, and M. J. Thoraval, Phys. Rev. Lett. **124**, 184501 (2020).
3 D. Lohse, B. Schmitz, and M. Versluis, Nature **413**, 477 (2001).
4 D. C. Woods, J. S. Bolton, and J. F. Rhoads, J. Acoust. Soc. Am. **138**, 2062 (2017).
5 E. Bok, J. J. Park, H. Choi, C. K. Han, O. B. Wright, and S. H. Lee, Phys. Rev. Lett. **120**, 044302 (2018).
6 T. Lee, and H. Iizuka, Phys. Rev. B **102**, 104105 (2020).
7 C. Liu, C. Ma, X. Li, J. Luo, N. X. Fang, and Y. Lai, Phys. Rev. Appl. **13**, 054012 (2020).
8 J. J. Park, K. J. B. Lee, O. B. Wright, M. K. Jung, and S. H. Lee, Phys. Rev. Lett. **110**, 244302 (2013).
9 Z. Zhang, Q. Zhu, C. Song, and W. Jiang, Sci. China-Phys. Mech. Astron. **68**, 254302 (2025).
10 Z. Huang, Z. Zhao, S. Zhao, X. Cai, Y. Zhang, Z. Cai, H. Li, Z. Li, M. Su, C. Zhang, et al., ACS Appl. Mater. Interfaces **13**, 53242 (2021).
11 C. Guidolin, J. Mac Intyre, E. Rio, A. Puisto, and A. Salonen, Nat. Commun. **14**, 1125 (2023).
12 K. Langley, E. Q. Li, and S. T. Thoroddsen, J. Fluid Mech. **813**, 647 (2017).
13 S. Xie, H. Ma, J. Cao, F. Mo, Q. Cheng, Y. Li, and T. Hao, Sci. China-Phys. Mech. Astron. **67**, 274311 (2024).
14 S. Zhu, A. Kherbeche, Y. Feng, and M. J. Thoraval, Phys. Fluids **32**, 041705 (2020).
15 Z. Fang, K. Wan, and M. E. Taslim, Droplet **3**, e123 (2024).
16 F. Chen, A. Xu, J. Song, Y. Gan, Y. Zhang, and N. Guan, Sci. China-Phys. Mech. Astron. **67**, 124611 (2024).
17 F. Omota, A. C. Dimian, and A. Bliek, Chem. Eng. Sci. **61**, 823 (2006).
18 D. Dedovets, Q. Li, L. Leclercq, V. Nardello-Rataj, J. Leng, S. Zhao, and M. Pera-Titus, Angew. Chem. Int. Ed. **61**, e202107537 (2022).
19 X. Ji, X. Wang, Y. Zhang, and D. Zang, Rep. Prog. Phys. **83**, 126601 (2020).
20 M. Zhang, and P. Guiraud, Water Res. **126**, 399 (2017).
21 A. M. Zhang, S. M. Li, P. Cui, S. Li, and Y. L. Liu, Sci. China-Phys. Mech. Astron. **66**, 124711 (2023).
22 T. Kudo, K. Sekiguchi, K. Sankoda, N. Namiki, and S. Nii, Ultrason. Sonochem. **37**, 16 (2017).
23 W. J. Xie, and B. Wei, Appl. Phys. Lett. **79**, 881 (2001).
24 M. A. B. Andrade, N. Pérez, and J. C. Adamowski, Braz. J. Phys. **48**, 190 (2018).
25 M. Baudoin, and J. L. Thomas, Annu. Rev. Fluid Mech. **52**, 205 (2020).
26 F. Lemoult, M. Fink, and G. Lerosey, Phys. Rev. Lett. **107**, 064301 (2011).
27 C. Ding, H. Chen, S. Zhai, S. Liu, and X. Zhao, J. Phys. D-Appl. Phys. **48**, 045303 (2015).
28 D. Foresti, M. Nabavi, M. Klingauf, A. Ferrari, and D. Poulikakos, Proc. Natl. Acad. Sci. USA **110**, 12549 (2013).
29 X. Ji, P. Jiang, Y. Jiang, H. Chen, W. Wang, W. Zhong, X. Zhang, W. Zhao, and D. Zang, Adv. Sci. **10**, 2300049 (2023).
30 Y. Zhang, Y. Han, X. Ji, D. Zang, L. Qiao, Z. Sheng, C. Wang, S. Wang, M. Wang, Y. Hou, et al., Nature **610**, 74 (2022).
31 L. Chen, L. O. Heim, D. S. Golovko, and E. Bonaccurso, Appl. Phys. Lett. **101**, 031601 (2012).
32 J. Möller, and T. Narayanan, Phys. Rev. Lett. **118**, 198001 (2017).
33 D. Zang, L. Li, W. Di, Z. Zhang, C. Ding, Z. Chen, W. Shen, B. P. Binks, and X. Geng, Nat. Commun. **9**, 3546 (2018).
34 S. T. Thoroddsen, K. Takehara, H. D. Nguyen, and T. G. Etoh, J. Fluid Mech. **848**, R3 (2018).
35 M. P. Brenner, Nature **403**, 377 (2000).
36 V. Duclaux, F. Caillé, C. Duez, C. Ybert, L. Bocquet, and C. Clanet, J. Fluid Mech. **591**, 1 (2007).
37 C. Duez, C. Ybert, C. Clanet, and L. Bocquet, Nat. Phys. **3**, 180 (2007).
38 N. S. Dickey, and A. Selamet, J. Sound Vib. **195**, 512 (1996).